Unstable higher modes of a three-dimensional nonlinear Schrödinger equation

Darran E. Edmundson
Research Center for Computational Science, Fujitsu Ltd., 1-9-3 Nakase, Mihama-ku, Chiba 261, Japan
(Received 20 January 1997)

Characterized by a central core surrounded by a number of concentric shells, the stability of the higher-bound solitary wave solutions to a three-dimensional nonlinear Schrödinger equation with saturating nonlinearity is investigated. A linear stability analysis of spherical harmonic modes reveals these solutions to be transversely unstable. Further, the complicated intermediate patterns observed in numerical simulations are shown to result from a degeneracy in the number of maximally unstable modes, the mode mixture depending on the realization of the destabilizing perturbation. [S1063-651X(97)00106-2]

PACS number(s): 42.65.Tg, 42.65.Sf

I. INTRODUCTION

The generalized nonlinear Schrödinger (NLS) equation

$$i\frac{\partial E}{\partial z}+\frac{1}{2}\nabla^2 E+f(|E|^2)E=0 \tag{1}$$

is a d-dimensional amplitude equation that describes the modulations of a slowly varying complex envelope E in the presence of weak nonlinearity governed by the function $f(|E|^2)$. It arises quite naturally in several physical contexts [1], for example, the evolution of the plane-polarized envelope of a quasimonochromatic electromagnetic pulse propagating through a dielectric having an intensity-dependent dielectric constant [2]. In one dimension with $f(|E|^2)=|E|^2$, Eq. (1)'s most well-known attribute is its integrability and the analytical existence of soliton solutions [3]. For the same nonlinearity in $d>1$ dimensions, while localized solitary wave solutions exist, they are found to be unstable to small perturbations, the pulses either delocalizing or undergoing collapse depending on the initial condition. As noted by Wilcox and Wilcox [4], this is a relatively common occurrence, ''except for the case of one dimension, wave functions obtained from equations containing low-order nonlinearities generally suffer from the disease of being unstable . . . .'' However, in numerous cases it has been found that saturation of the nonlinearity suppresses the instability resulting in the existence of stable (at least to small perturbations) localized solutions.

As illustrative examples, the stabilizing effect of nonlinear saturation was invoked by Marburger and Dawes [5] in the early days of nonlinear optics to explain the formation of small-scale filaments in the cross section of a self-focusing laser beam, by Wilcox and Wilcox [4] and Kaw *et al.* [6], who considered a saturating exponential nonlinearity in a class of two- and three-dimensional (3D) wave equations, and more recently in the study of ''light bullets''—stable 3D nondispersing nondiffracting optical envelope solitons [7–10].

In addition to the fundamental Gaussianlike stationary states that only asymptotically approach zero, in $d>1$ there exist higher-bound solitary waves that are characterized by progressively less localization and, more importantly, an increasing number of field nodes (zero intercepts of $|E|$). Recently, Soto-Crespo *et al.* [11] studied the stability of these higher-bound states in a 2D NLS equation with saturating nonlinearity. In this case, the fundamental mode is a single Gaussian-like peak while the higher modes are comprised of a central spot surrounded by a number of concentric rings. Numerical propagation of these solitary waves revealed them to be transversely unstable, the rings decomposing into a number of stable filaments that subsequently underwent complicated dynamical interactions. The number of filaments formed by a given ring was found to agree with the predictions of both a linear stability analysis and an approximate analytical treatment.

The aim of this paper is to investigate the analogous case in three spatial dimensions. Using the terminology of nonlinear optics, here the fundamental mode is a stable spherically symmetric ''light bullet'' while the higher-bound states consist of an inner core surrounded by a number of concentric shells. Not surprisingly, these higher modes are also found to be unstable to propagation, the shells eventually decaying into a number of fundamental light bullets. However, due to both the increased dimensionality and a degeneracy in the number of unstable modes possessing the maximal growth rate, the nature of this decay is markedly different from the 2D case.

The remainder of the paper is organized as follows. In Sec. II, the model equation is introduced from a nonlinear optics perspective and the solitary wave solutions are described. In Sec. III, the linear stability analysis formalism is presented and predictions are made about the expected dynamical behavior of shell-state propagation under the governing wave equation. In Sec. IV, simulations are shown for the one- and two-shell cases and the results examined in view of the linear stability analysis predictions. Finally, Sec. V contains a summary and brief discussion.

II. MODEL EQUATION AND STATIONARY STATES

The physical situation we consider is the propagation of a 3D plane-polarized quasimonochromatic electromagnetic pulse traveling through a bulk nonlinear glass under the combined effects of dispersion and diffraction. With the assumption that the pulse envelope ϕ is slowly varying compared to the carrier frequency and that the intensity-dependent refractive index has the saturable form $n=$

$n_0+n_2|\phi|^2/(1+a'|\phi|^2)$, where a' is an inverse measure of the saturation intensity, the complex envelope evolves according to [7]

$$2ik\left(\frac{\partial}{\partial z'}+\frac{1}{v_g}\frac{\partial}{\partial t'}\right)\phi+\frac{\partial^2\phi}{\partial x'^2}+\frac{\partial^2\phi}{\partial y'^2}+kD\frac{\partial^2\phi}{\partial t'^2}+\frac{2k^2n_2}{n_0}\frac{|\phi|^2}{(1+a'|\phi|^2)}\phi=0. \quad (2)$$

Here, z' is the pulse propagation direction, x' and y' the transverse spatial dimensions, t' the time, k the wave vector of the underlying carrier wave, v_g the group velocity, and D (assumed positive) the group velocity dispersion. Making use of the scalings $t=(t'-z'/v_g)(k/D)^{1/2}$, $(x,y,z)=k(x',y',z')$, $E=(n_2/n_0)^{1/2}\phi$, and $a=(n_2/n_0)a'$, we obtain the following (3+1)-dimensional nonlinear Schrödinger equation:

$$i\frac{\partial E}{\partial z}+\frac{1}{2}\nabla^2E+\frac{|E|^2}{1+a|E|^2}E=0, \quad (3)$$

where $\nabla^2\equiv\partial^2/\partial t^2+\partial^2/\partial x^2+\partial^2/\partial y^2$. Note the existence of only one free parameter implying that, even restricting ourselves to the current physical context, the results that follow are applicable to a wide range of material and pulse parameters.

Spherically symmetric solitary wave solutions (spheroidal in laboratory units) are found by inserting the assumed form

$$E(r=\sqrt{t^2+x^2+y^2},z)=\exp(i\beta z)U(r) \quad (4)$$

into Eq. (3) yielding an ordinary nonlinear differential equation for the radial profile, viz.,

$$\frac{d^2U}{dr^2}+\frac{2}{r}\frac{dU}{dr}+2U\left[\frac{U^2}{1+aU^2}-\beta\right]=0. \quad (5)$$

Assuming that U has its maximal value at $r=0$, and imposing the boundary conditions dU/dr, $d^2U/dr^2\to 0$ as $r\to\infty$, Eq. (5) constitutes a two-point boundary value problem for the real profile U. Lacking an analytical solution, these radial profiles must be obtained numerically, one empirically finding a single monotonically decreasing Gaussian-like profile and a number of higher modes characterized by an increasing number of $U=0$ crossings of the field. The members of a given β family are enumerated U_n where the subscript n denotes the number of zero crossings.

As an example, setting the saturation parameter $a=0.05$ (which it will remain for the remainder of this paper), Fig. 1 shows the lowest three modes from the $\beta=3$ family of solutions. Profiles at other β values are qualitatively similar, this parameter's effect being to gradually modify both the field's peak height and the locations and depths of the extrema. As the simulation results presented later depict the evolution of the modulus of the complex field E, the figure inset similarly shows $|E_1|=|U_1|$ revealing a central core surrounded by a single shell.

As intimated in the Introduction, the simple existence of solitary wave solutions does not imply their stability when evolved under the governing wave equation. Some insight into stability can be obtained as follows. For a given profile

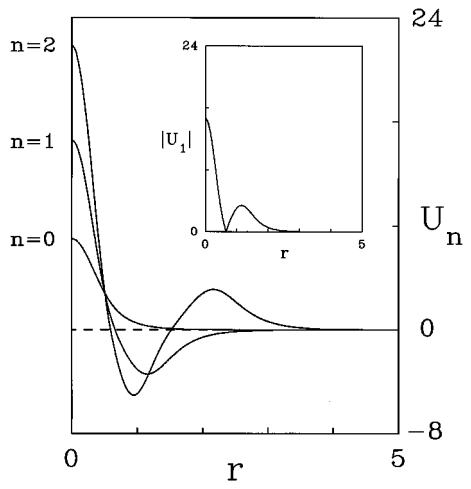

FIG. 1. The lowest three modes from the $\beta=3$ family of solitary wave solutions. Inset: modulus of the U_1 solution reveals a central core surrounded by a single shell.

$U_n(r;\beta)$, the integrated intensity (power) of the nth mode as a function of the (shape-changing) parameter β is given by

$$P_n(\beta)=\int_0^\infty U_n(r;\beta)^2r^2dr. \quad (6)$$

Figure 2 shows the power curves for the lowest three modes where the filled circles indicate the powers of the three solutions depicted in Fig. 1. The general U shape of these curves is characteristic of $f(|E|^2)$ models displaying saturable behavior. Further, the minima of the P_0 curve (denoted $P_{\min}$) is found to delimit two regions of differing stability. Solitary waves on the negative slope branch are numerically found to be unstable [10]. Conversely, positive slope solitary waves are theoretically predicted to be stable [12] and this is borne out by numerical simulations [10,13]. In addition to their intrinsic stability, these solutions have been shown to act as attractor states to initial profiles quite different from

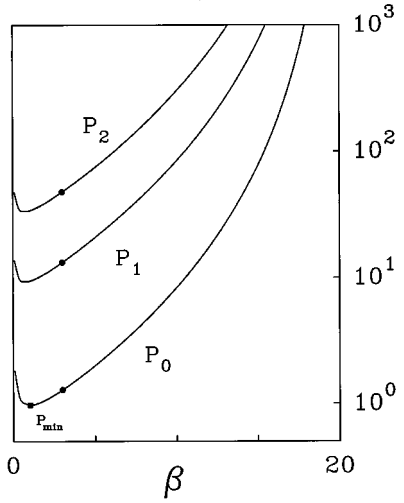

FIG. 2. Integrated intensity (power) vs the shape-changing parameter β for the lowest three bound modes. Circles correspond to the profiles shown in the preceding figure. Solitary waves to the right of $P_{\min}$ are known to be stable.

the true solitary wave profile, e.g., Akhmediev and Soto-Crespo have demonstrated the decay of a cylindrical beam subject to a temporal modulation into a train of fundamental states [8].

One might initially suspect that the higher modes also obey the above stability criterion and that stable shell states are viable for a range of positive-slope β values. However, this test does not preclude the existence of a transverse instability, a situation which was observed in Ref. [11] in a 2D version of Eq. (3) and which we similarly investigate for $d=3$.

III. LINEAR STABILITY ANALYSIS

In this section a linear stability analysis is performed for the 3D shell states. Section III A discusses the method used to determine the growth rates and functional forms of the unstable perturbation eigenmodes. The subsequent sections present linear stability analysis results for the one- and two-shell cases, respectively.

A. Formalism

To analyze the stability of the shell states, we follow Soto-Crespo *et al.* [11] and, considering the Laplacian of Eq. (3) in spherical polar coordinates, choose an appropriate separable perturbation to the nth mode stationary solution E_n, namely,

$$E(r,\theta,\phi,z)=E_n(r,z)+\mu g(r,z)Y_l^m(\theta,\phi). \tag{7}$$

Here, μ is a small expansion parameter and, noting that the angular perturbation function must be real to obtain the linearized equation that follows, the spherical harmonic function is defined as $Y_l^m(\theta,\phi)=P_l^m(\theta)\cos(m\phi)$, with P_l^m the associated Legendre function.

To first order in μ, substitution of Eq. (7) into Eq. (3) yields the following (linear) partial differential equation for the radial evolution of a given perturbation

$$i\frac{\partial g}{\partial z}+\frac{1}{2r^2}\frac{\partial}{\partial r}\left(r^2\frac{\partial g}{\partial r}\right)-\frac{l(l+1)}{2r^2}g + \frac{2|E_n|^2g+a|E_n|^4g+E_n^2g^*}{(1+a|E_n|^2)^2}=0. \tag{8}$$

While the θ dependence is implicit via the spherical harmonic mode index l, due to rotational invariance of the Laplacian no reference to the azimuthal index m occurs in Eq. (8). The ramifications of this point will become clear in Sec. III B.

Exponentially growing solutions of the form

$$g(r,z)=g(r)\exp(\delta z) \tag{9}$$

are sought with substitution of Eq. (9) into Eq. (8) constituting an eigenvalue problem for the growth constant δ and radial perturbation eigenfunction $g(r)$. Rather than solve this problem directly, the following technique due to Akhmediev *et al.* [14] was used to extract both the perturbation eigenfunctions and their respective growth rates. If the system possesses exponentially growing solutions then a random initial profile evolved numerically according to Eq. (8) should eventually be dominated by the mode with the largest growth rate. Once this mode emerges, the growth constant can be extracted via the prescription

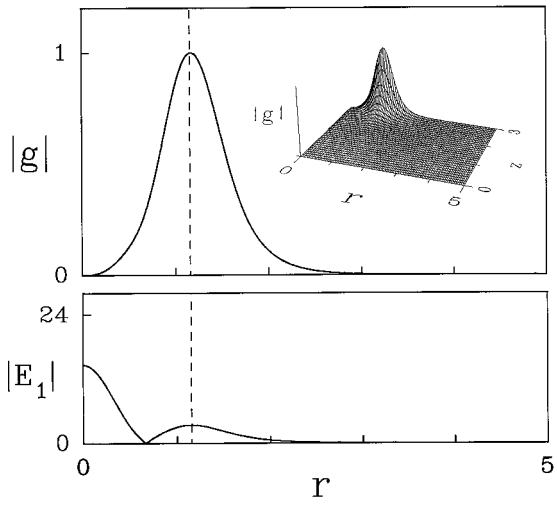

FIG. 3. Top: dominant unstable $l=3$ radial perturbation eigenmode emerging from a small random initial condition. Bottom: modulus of the $\beta=3$ one-shell solitary wave.

$$\delta_l=\frac{1}{\Delta z}[\ln|g(r,z+\Delta z)|-\ln|g(r,z)|] \tag{10}$$

and the calculation terminated when δ_l converges both in z and as calculated at several locations across the pulse. This latter stopping criterion ensures that $g(r)$ is growing in a spatially invariant way and is an accurate representation of the true radial perturbation eigenfunction.

B. One-shell case

As a concrete example, consider the stability of the $\beta=3$ one-shell state depicted in Fig. 1 to a spherical harmonic perturbation with index $l=3$. Starting with a small random initial condition for $g(r,0)$, Eq. (8) was evolved using a (unconditionally stable) Crank-Nicholson algorithm [15]. As shown in the inset of Fig. 3, an exponentially growing radial profile for $|g|$ emerges. The vertical scale is omitted as the absolute height of the pulse is not important. Rather, the salient feature is that by $z=3$ all points across the pulse are found to be growing at the same exponential rate $\delta_3=3.75$. At this point the calculation was terminated yielding the (normalized) $|g(r)|$ profile shown to the left of the inset figure. For comparison, below we plot the $\beta=3$ one-shell radial profile revealing that $|g|$ is peaked about the mean radius of the shell and acts negligibly in the vicinity of the origin. Such localization implies that this perturbation will affect only the shell leaving the central core relatively untouched.

In order to discover the maximally unstable mode, the above analysis was repeated for other l values, one finding that aside from the unstable mode discussed above, only for $l=1$, 2, and 4 do exponentially growing profiles emerge. These unstable modes possess growth rates of $\delta_l=0.54$, 3.15, and 2.73, respectively, and have radial eigenfunctions

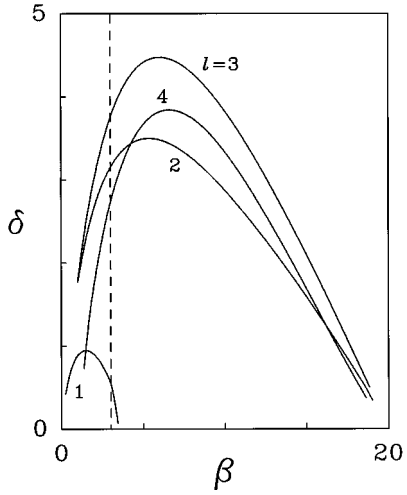

FIG. 4. Unstable mode growth rates for the complete spectrum of one-shell states. The vertical dashed line corresponds to the $\beta=3$ case discussed in the text.

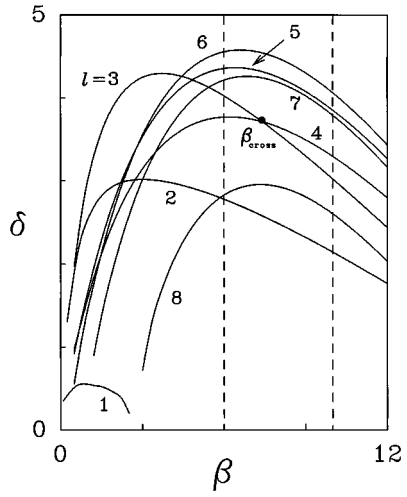

FIG. 5. Unstable growth rates for the spectrum of two-shell states. (The range $12<\beta<20$ has been omitted to ease viewing of the myriad of curves.)

qualitatively similar to that shown in Fig. 3. The other families thus possess either negative or purely imaginary eigenvalues and will not influence the dynamics of the initial breakup. In decreasing order of instability, the ranking of the growth rates is $l=3$, 2, 4, and 1 and we therefore predict that the initially symmetric shell will evolve into a structure characteristic of the maximally unstable $l=3$ mode. (As noted in Ref. [11] for the $d=2$ case, this ordering of modes conflicts with the findings of Kolokolov and Sykov [16] who predicted that the unstable mode with the largest l index would be maximally unstable.)

In the $d=2$ case, angular perturbations were chosen of the form $\cos(m\phi)$ and an analysis similar to that above yielded a single m value for the maximally unstable growth mode. Numerical simulations then showed the outer ring decomposing into m angularly equispaced spots. The situation in $d=3$ is more complicated for two reasons. First, to perhaps state the obvious, recognizing a given pattern as a manifestation of a particular spherical harmonic is not a trivial visual task. Second, and more important, since Eq. (8) contains no reference to the azimuthal index m, a theoretical degeneracy exists and four $l=3$ spherical harmonic modes can possibly be present: Y_3^0, Y_3^1, Y_3^2, and Y_3^3. This raises an interesting question, namely, is one mode selected preferentially or does a linear combination of allowable modes emerge, the mixture depending on the realization of the noise used to provoke the system out of its unstable state? We address this issue empirically in Sec. IV with a series of numerical experiments followed by spectral analysis of the simulation data.

The analysis carried out above pertains only to the $\beta=3$ state. Repeating this procedure for all solitary waves in the range of allowable β results in the growth rate curves depicted in Fig. 4. Here the key feature is that the $l=3$ mode is maximally unstable regardless of the choice of the parameter β. This is in contrast to the $d=2$ case, where the $m=3$ and $m=4$ curves intersect at an intermediate β value, the crossover point dividing the spectrum of states into two classes whose long-term evolution displayed either threefold or fourfold symmetry.

C. Two-shell case

Repeating the above procedure for the spectrum of two-shell states, Fig. 5 shows the corresponding unstable growth rate curves. Consider first the $\beta=6$ case indicated by the left-most dashed line. Maximally unstable is the $l=6$ mode followed in descending order by $l=5$, 7, 3, 4, 8 and 2. The solid curves at the top of Fig. 6 show the radial perturbation functions corresponding to the $l=6$ and $l=3$ modes. Although $l=6$ is maximally unstable, $|g|$ corresponding to this mode is concentrated at the outer shell and acts negligibly at smaller radii. As the radial perturbation functions for $l=5$ and $l=7$ are qualitatively similar, the first mode that acts significantly on the inner shell is the $l=3$ mode. Therefore, one expects markedly different patterns to appear as the two shells break symmetry and decompose.

The dotted curve in Fig. 6 shows the $l=4$ radial perturbation function. Although this mode is localized mainly about the outer shell, it also possesses a small peak at the inner-halo radius. While this perturbation is not maximally unstable for lower β values, above the crossover point indi-

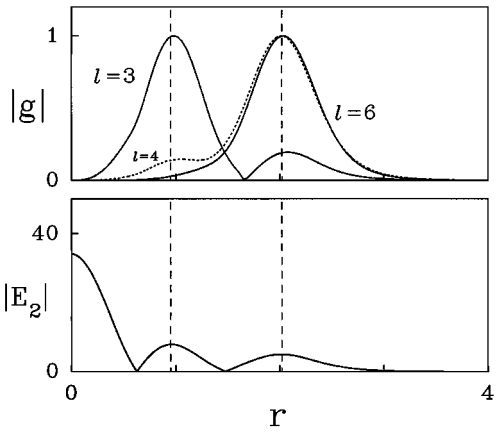

FIG. 6. Top: sample radial perturbation eigenfunctions for the $\beta=6$ two-shell case. Bottom: modulus of the $\beta=6$ two-shell solitary wave.

cated by the solid circle in Fig. 5, the $l=4$ growth rate exceeds that of the $l=3$ mode. In this region, the $g(r)$ are qualitatively similar to those of Fig. 6 (the $l=4$ shoulder slowly diminishing with increasing β) and so β_{cross} should divide the spectrum of states into two classes possessing different inner-shell stability properties. However, it is not *a priori* evident that the small $l=4$ shoulder is sufficient to dominate the sharply peaked $l=3$ mode having only a slightly lower growth rate. Thus, for the $\beta=10$ case indicated by the right-most vertical dashed line in Fig. 5, the outer shell should (still) display a Y_6^m-type instability with the inner shell possibly decaying into a pattern reflecting the Y_4^m family of modes.

IV. NUMERICAL RESULTS

To test the predictions of Sec. III, one- and two-shell solitary wave profiles were numerically evolved according to Eq. (3). In Sec. IV A, the particulars of the numerical techniques utilized are described. In Sec. IV B typical one-shell simulations are presented and the results interpreted via a spherical harmonic spectral analysis at varying stages of the solitary wave's decay. Section IV C presents an analogous treatment of the two-shell case.

A. Numerical methods

While the linear stability analysis was carried out in spherical polar coordinates, the numerical code used to evolve solitary waves according to Eq. (3) was that used for previous interaction studies [9,13,17] where a Cartesian coordinate system was the most natural choice. Solitary wave solutions were centered on a 128^3 (t,x,y) mesh and evolved forward in z using the beam-propagation method (BPM) [18], a split-operator algorithm consisting of alternating stages of linear and nonlinear evolution. The advantage of this technique is the tremendous speed increase that one realizes from solving the linear problem in the Fourier domain with a highly efficient (and vectorizable) fast fourier transform (FFT) algorithm [19]. The accuracy of the solution was checked by repeating the simulations with different ''time-step'' values Δz.

As mentioned earlier, recognizing the decomposition of an initially symmetric shell into a pattern reflecting a particular spherical harmonic is an arduous visual task. Therefore, a quantitative spectral analysis of $|E|$ was performed using the SPHEREPACK library [20]. This package is able to determine the harmonic coefficients A_l^m and B_l^m in the expansion

$$|E(r^*,\theta_i,\phi_j)| = \sum_l \sum_m [A_l^m \cos(m\phi_j) - B_l^m \sin(m\phi_j)] P_l^m(\theta_i), \tag{11}$$

where θ_i and ϕ_j define a spherical mesh at the radius r^* and P_l^m is the associated Legendre function that appeared in the definition of the spherical harmonic. As the simulation data is defined on a Cartesian grid, interpolation of $|E|$ from the regular mesh (t,x,y) to the locations (r^*,θ_i,ϕ_j) is required. In addition, one must also choose a pole with respect to which the θ_i are oriented. The harmonic analysis is affected by such a choice and so the pole is selected on a case by case basis to align with an obvious symmetry axis of the broken state. Finally, rather than considering the evolution of both A and B, note that $C\equiv\sqrt{A^2+B^2}$ is invariant to rotations about the pole. As the absolute orientation is of little interest, consideration of the C_l^m will suffice.

B. One-shell simulations

Consider the decomposition of the $\beta=3$ one-shell solitary wave. As a slight modification to the $U(r)$ profile, a small random noise term Γ is added in order to seed the instability, viz.,

$$E(r,z=0)=U(r)[1+\Gamma(t,x,y)]. \tag{12}$$

Although the solitary wave is unstable without this modification due simply to the presence of intrinsic numerical noise, in such cases one finds that the evolving solution possesses the symmetry of the underlying computational mesh. With the addition of a destabilizing perturbation intended to mimic the fluctuations inherent to a real system, this effect disappears and one is properly left with a symmetry breaking determined by the physics of the problem.

Figure 7 shows volume-rendered images of $|E|$ at six interesting stages of the evolution [21]. (Note that the crisp edges in these images are an artifact of the visualization process, $|E|$ values below this surface level being rendered transparent.) From $z=0$ to approximately $z=2.0$ (not shown) the initial state remains relatively stable. However, by frame (b) the shell has become slightly aspherical and begun to clump in two regions. In frame (c) this process is well developed and the shell has coalesced into a tubelike structure and single ''ball.'' In agreement with the localization of the unstable radial perturbation functions, the central core remains relatively unaffected by these transverse instabilities. As the ball in the foreground begins to move towards the lower-front corner of the mesh, the tube structure drifts in the opposite direction slowly expanding in diameter. In frames (d) and (e), the tube is observed to pinch off at several locations forming four separated clumps. Referring to the power curves of Fig. 2, the left-most clump does not possess enough energy content to form a fundamental soliton (i.e., $P<P_{\text{min}}$) and therefore disperses into the background. Demonstrating the attractorlike nature of the fundamental state, a one-parameter fit in β of their respective radial intensity profiles (not shown) indicates that the other objects have condensed into E_0 light bullets. In the final image, the bottom-right light bullet pokes through the back wall as it transits the periodic boundary implicit to the numerical scheme.

Taking SPHEREPACK's orientational pole to align with the obvious cylindrical symmetry axis of Fig. 7(c), and with the north pole deemed to be at the bottom-front of the image to facilitate later discussion, Fig. 8 shows the z evolution of the spherical harmonic decomposition of $|E|$ at the mean radius of the shell $r^*=1.15$. The data is restricted to $l\leqslant 5$, as modes above this value are found to contain negligible energy content. In addition, due to its large initial value, the dc mode Y_0^0 is omitted from this figure. (C_0^0 does, however, decrease rapidly in the vicinity of $z=3.0$ as the tube and the lower-

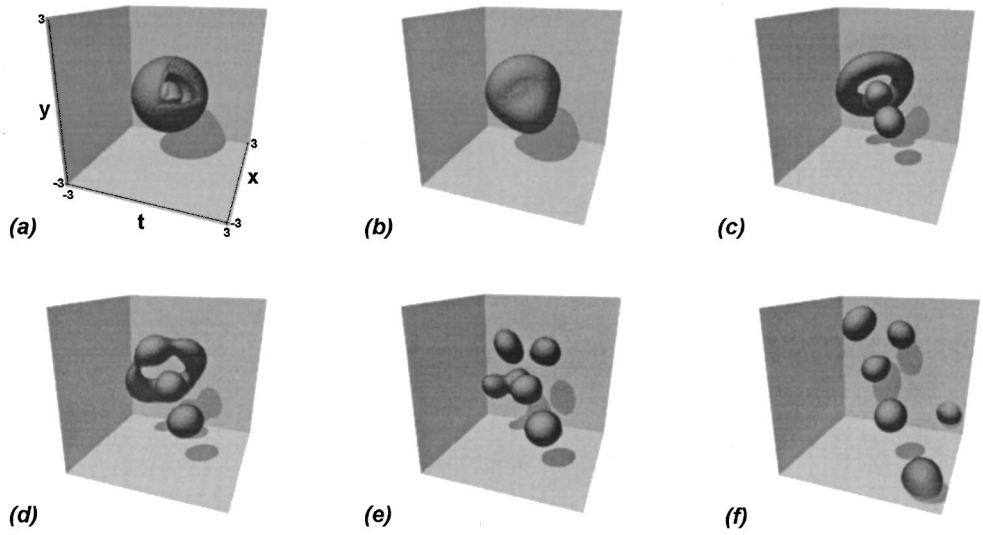

FIG. 7. Simulation of the $\beta=3$ one-shell state reveals instability of the solution to a small amount of random noise. (a) $z=0$, (b) $z=2.4$, (c) $z=2.8$, (d) $z=3.2$, (e) $z=3.4$, and (f) $z=4.6$. [In frame (a) an octant has been removed in order to visualize the central core.]

forming bullet move away from the analysis radius.) As predicted, an $l=3$ mode dominates the initial evolution, at least up until the formation of the torus structure which is already far beyond the linear regime.

The correspondence between the dominant Y_3^0 mode and the pattern that emerges out of the originally symmetric shell is readily understood by referring to the $P_3^0(\theta)$ associated Legendre function, shown in Fig. 9. At angular locations where P_3^0 is positive (negative), $|E(r\simeq r^*)|$ tends to increase (decrease) in intensity. Thus, the peak at $\theta=0$ leads to coalescence of the light bullet at the north pole, the maxima near $\theta=0.6\pi$ results in the formation of the tube structure, and the bracketed negative minima causes field depletion in the intervening region. The lack of any field intensity above the tube is a result of the P_3^0 minima near $\theta=\pi$.

Repeating this simulation with different realizations of the random noise term, one observes a variety of other patterns characterized by various mixtures of Y_3^m modes. Thus rather than the Y_3^0 pure state being intrinsically favored by the system, the structure of Fig. 7(c) is likely the result of a bias in the destabilizing noise. Unfortunately, since a SPHEREPACK analysis of the noise depends upon the radius at which it is calculated, correlation with the emergent pattern is difficult. While this problem could be avoided by performing simulations on a spherical mesh, where the perturbation can trivially be made radially invariant, instead we choose a different approach. Namely, we investigate the patterns that emerge when the perturbation is intentionally biased towards a specific mode or combination of modes from the maximally unstable family.

For example, if the (small) destabilizing perturbation consists solely of the Y_3^2 mode (having its orienting pole perpen-

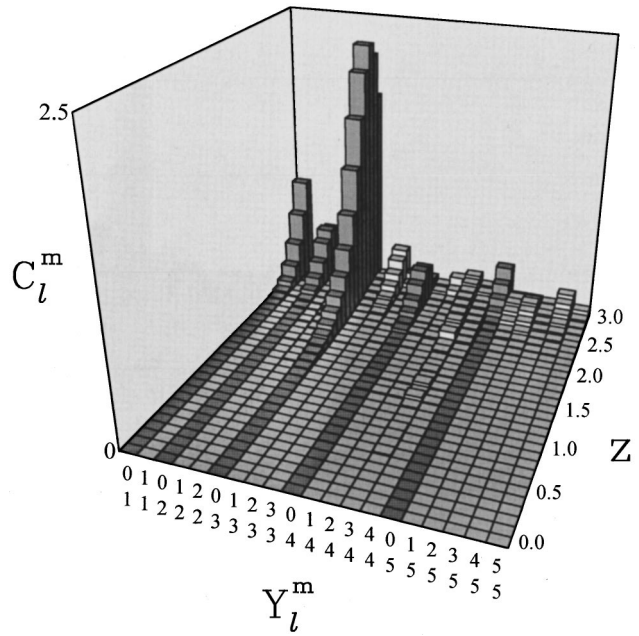

FIG. 8. Spherical harmonic spectral analysis of the simulation data of Fig. 7. Dominance of an $l=3$ mode confirms the predictions of Fig. 4.

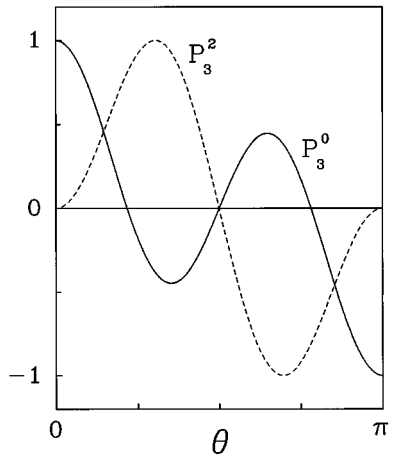

FIG. 9. Associated Legendre functions used to explain the formation of one-shell patterns discussed in the text. (The P_l^m have been vertically scaled to fit on the same viewgraph.)

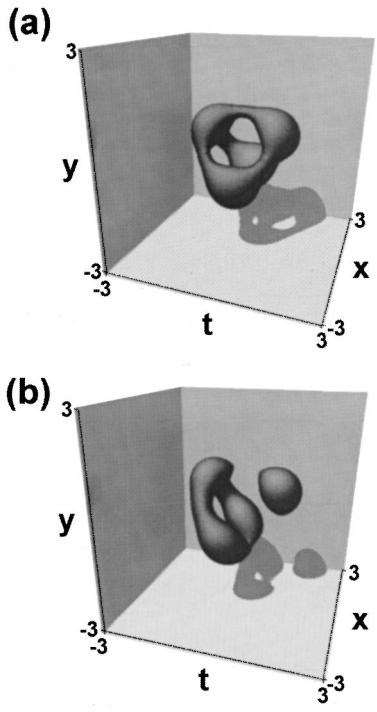

FIG. 10. Intermediate structures that emerge when the destabilizing perturbation is biased towards specific mode(s). (a) Y_3^2 only. (b) A particular linear combination of all Y_3^m modes. (The inner core has been removed for clarity.)

dicular to the t-x plane), the radically different pure-state structure of Fig. 10(a) emerges. [Referring to P_3^2 shown in Fig. 9, this pattern can be understood with an argument analogous to that above, taking into account the effect of the $\cos(2\phi)$ azimuthal perturbation function.] Different pure-state patterns can similarly be achieved for the remaining Y_3^1 and Y_3^2 modes. In addition, when the initial perturbation consists of an arbitrary linear combination of modes, this *same* mode mixture is observed in a spectral analysis of the emergent structure. As an illustrative example, Fig. 10(b) shows a volume rendering of the intermediate pattern that develops from a destabilizing perturbation in the ratio $(Y_3^0:Y_3^1:Y_3^2:Y_3^3)=(4:3:2:1)$. Although this pattern is observed in a regime far removed from that where the linear stability analysis is valid, spectral analysis recovers the above ratios to within $\pm 5\%$. Further, preservation of the initial mode mixture is found to be insensitive to both the magnitude of the perturbation and the purity of the initial spectrum as qualitatively similar results are obtained when the perturbation is both decreased in strength and augmented with random noise.

C. Two-shell simulations

We turn now to the more complicated two-shell case. Figure 11 shows the result of numerically propagating the $\beta=6$ two-shell state in the presence of a small amount of random noise. Between $z=0$ and $z=1.3$ (not shown) little change occurs in the initial solitary wave. By frame (b), the outer shell has evolved into a structure where light bullets are coalescing at the vertices of apparently hexagonal faces. Note, however, that while the symmetry breaking of the outer shell is well advanced, the inner shell remains relatively intact. By frame (c), the outer-shell structure has completely disintegrated resulting in the formation of a multitude of interacting E_0 light bullets. At this point the inner shell begins to decompose although the small scale and surrounding matter make it difficult to discern the nature of the emerging pattern. In the remaining frames, the light bullets move radially outwards towards the mesh boundaries undergoing complicated dynamical interactions. [As an interesting aside, the two overlapping bullets indicated by the arrow in frames (c)–(f) coalesce, but then periodically emerge with oscillatory behavior reminiscent of a one-dimensional soliton breather mode.]

Consider the pattern formed by the outer shell localized about $r^*=2.0$. Taking the orientational pole to pierce through the center of the hexagonal face closest to the reader, Fig. 12(a) shows the resultant spherical harmonic decomposition of $|E(r^*)|$. In agreement with the linear stability predictions, the leading spectral component is a member of the

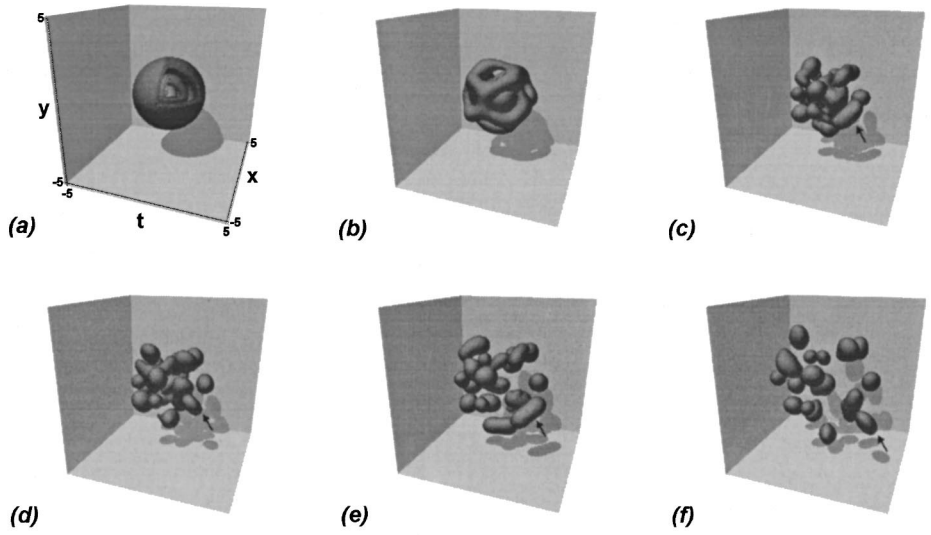

FIG. 11. Evolution of the $\beta=6$ two-shell state with random destabilizing noise. (a) $z=0$, (b) $z=1.9$, (c) $z=2.2$, (d) $z=2.4$, (e) $z=2.9$, and (f) $z=3.3$. [In frame (a) an octant has been removed in order to visualize both the central core and the inner shell.]

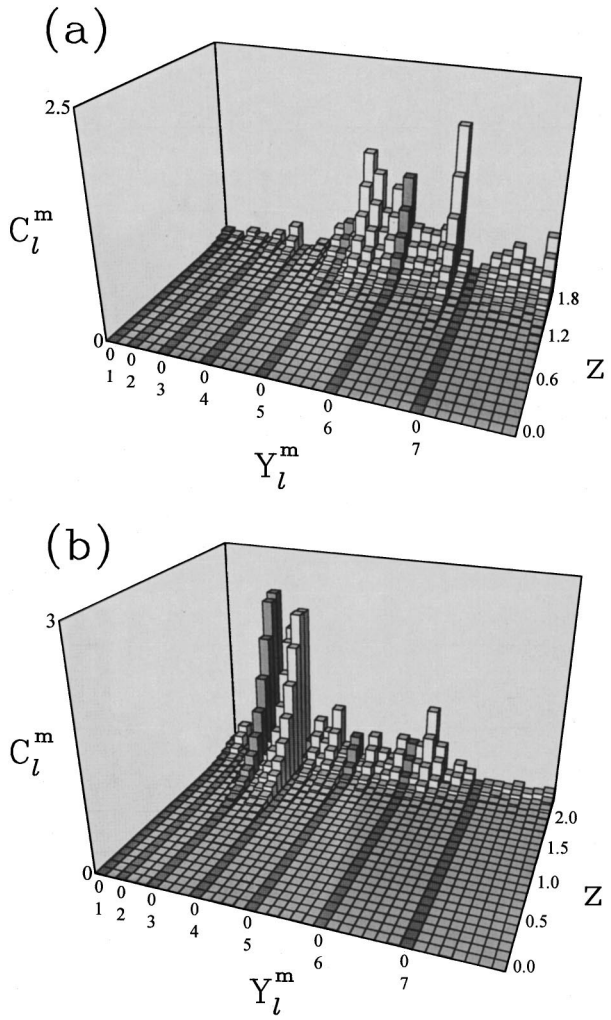

FIG. 12. Spherical harmonic spectral analysis of the simulation data of Fig. 11. (a) Outer shell. (b) Inner shell. (Axis labels for $m \neq 0$ modes have been omitted for clarity.)

$l=6$ family of modes. The reason for the significant spectral energy observed in the $l=5$ family is unclear but, noting that this mode's growth rate is only slightly lower than the dominant $l=6$ mode (see Fig. 5), is likely a result of a bias in the destabilizing perturbation [22]. Supporting evidence for this statement is twofold. First, repeating this simulation with different realizations of the random noise term, while the $l=6$ family is (as expected) always observed to dominate, a large $l=5$ contribution does not manifest itself in every simulation. Second, intentionally destabilizing with equal amounts of $l=5$ and $l=6$ modes (and taking into account the differing growth rates), this same mode mixture is observed in the emergent pattern.

To quantitatively analyze the $r^*=0.95$ inner-shell pattern, the surrounding matter in Fig. 11(c) was removed and an orientational pole identified. With such a choice, Fig. 12(b) shows the resultant harmonic analysis. In agreement with theory, the inner shell is dominated by the $l=3$ family of modes.

Repeating this simulation with different realizations of the random noise term, a myriad of complicated intermediate states characterized by various mixtures of $l=6$ outer-shell and $l=3$ inner-shell modes was observed. In addition, as in

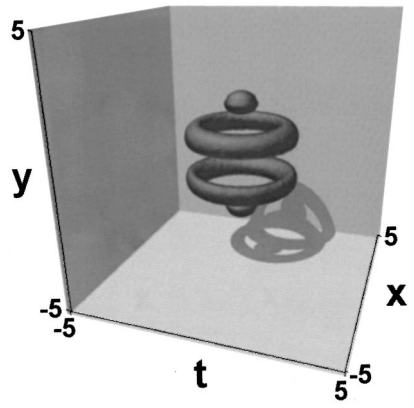

FIG. 13. Y_6^0 pure state obtained by biasing the destabilizing perturbation. (Both the inner shell and central core have been removed in this rendering.)

the one-halo simulations, pure-state patterns were produced by applying a small bias towards a particular mode, Fig. 13 showing the cylindrically symmetric Y_6^0 structure obtained via this technique. Further, evolution of the two-shell solitary wave was also found to preserve arbitrary mode mixtures used to destabilize the initial state, these small perturbations growing exponentially to determine the emergent intermediate pattern.

Finally, we consider the decay of the $\beta=10$ solitary wave's inner shell which, as discussed at the end of Sec. III C, may be dominated by an $l=4$ instability. Propagating this state in the presence of random noise, Fig. 14 shows the resultant harmonic decomposition of $|E|$ at the inner-shell radius $r^*=1.1$. While $l=4$ modes dominate the early evolution, beyond $z=2.5$ significant spectral content emerges in modes $l=3$ through $l=6$. This results in the formation of a highly irregular intermediate pattern (not shown) before the system eventually relaxes to a number of interacting fundamental states.

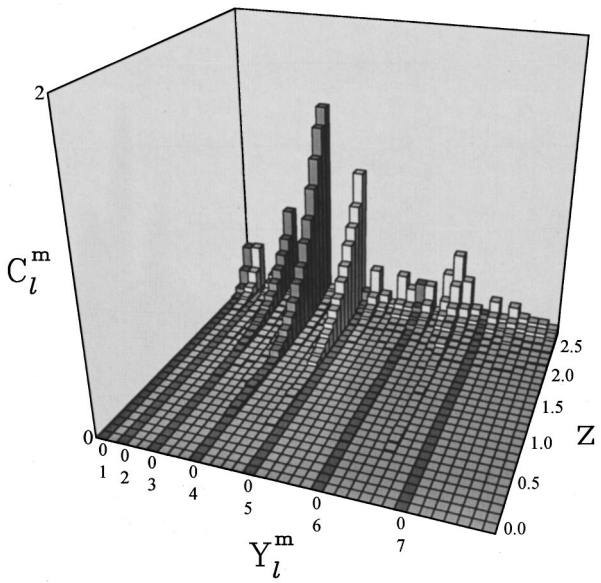

FIG. 14. Spherical harmonic spectral analysis of the $\beta=10$ two-shell state's inner halo.

V. CONCLUSION

In this paper, the transverse stability of the higher-bound solitary wave solutions of a 3D nonlinear Schrödinger equation with saturating nonlinearity was examined. A linear stability analysis of spherical harmonic modes Y_l^m showed these higher states to be unstable and yielded predictions for the maximally unstable family of modes expected to dominate the decay of each shell. Numerically evolving various one- and two-shell solitary waves in the presence of random noise intended to mimic the fluctuations inherent with a real system, these general predictions were confirmed by spectral analysis of the emergent patterns. However, in contrast with the $d=2$ case, rather than a single structure emerging independent of the realization of the random destabilizing perturbation, here a myriad of complicated intermediate patterns was observed. This was attributed to a degeneracy in the number of maximally unstable modes, all m members of a given l family being allowably present. Although a direct correlation between the random noise spectrum and the emergent mode mixture was not demonstrated, the ability to produce both pure states and arbitrary linear combinations of modes in the far-from-linear regime by appropriately biasing the destabilizing perturbation provides fairly conclusive evidence that such a connection exists.

[1] E. Infeld and G. Rowlands, *Nonlinear Waves, Solitons and Chaos* (Cambridge University Press, Cambridge, England, 1990).

[2] A. C. Newell and J. V. Maloney, *Nonlinear Optics* (Addison-Wesley, Redwood City, CA, 1992).

[3] V. E. Zakharov and A. B. Shabat, Sov. J. Theor. Phys. JETP **34**, 62 (1972).

[4] J. Z. Wilcox and T. J. Wilcox, Phys. Rev. Lett. **34**, 1160 (1975).

[5] J. H. Marburger and E. Dawes, Phys. Rev. Lett. **21**, 556 (1968).

[6] P. K. Kaw, K. Nishikawa, Y. Yoshida, and A. Hasegawa, Phys. Rev. Lett. **35**, 88 (1975).

[7] Y. Silberberg, Opt. Lett. **15**, 1282 (1990).

[8] N. Akhmediev and J. M. Soto-Crespo, Phys. Rev. A **47**, 1358 (1993).

[9] D. E. Edmundson and R. H. Enns, Phys. Rev. A **51**, 2491 (1995).

[10] R. McLeod, K. Wagner, and S. Blair, Phys. Rev. A **52,** 3254 (1995).

[11] J. M. Soto-Crespo, D. R. Heatley, E. M. Wright, and N. N. Akhmediev, Phys. Rev. A **44,** 636 (1991).

[12] A. A. Kolokolov, J. Appl. Mech. Tech. Phys. **3**, 426 (1973).

[13] D. E. Edmundson and R. H. Enns, Opt. Lett. **17,** 586 (1992).

[14] N. N. Akhmediev, V. I. Korneev, and Yu. V. Kuz'menko, Zh. Eksp. Teor. Fiz. **88**, 107 (1985) [Sov. Phys. JETP **61**, 62 (1985)].

[15] W. H. Press, B. P. Flannery, S. A. Teukolsky, and W. T. Vetterling, *Numerical Recipes* (Cambridge University Press, New York, 1986).

[16] A. A. Kolokolov and A. I. Sykov, J. Appl. Tech. Phys. **4**, 519 (1975).

[17] D. E. Edmundson and R. H. Enns, Opt. Lett. **18,** 1609 (1993).

[18] G. P. Agrawal, *Nonlinear Fiber Optics* (Academic, San Diego, 1989).

[19] Despite the intrinsic speed of the BPM, this three-dimensional problem still poses a significant computational burden. The simulations were carried out on Fujitsu VPX240/10 and VP2600 supercomputers.

[20] SPHEREPACK is available from the software repository Netlib, accessible via the World Wide Web at <URL: http://www.netlib.org/>.

[21] Animations of these and other simulations can be obtained at <URL: http://www.sfu.ca/~renns/lbullets.html>.

[22] The other possibility is that the ''dirty'' spectrum of Fig. 12(a) is an artifact of the mesh resolution. Unfortunately, dependence on a radix-2 FFT algorithm and the intensive memory and CPU requirements of simulating on a 256^3 grid prevented us from examining this possibility.